Mechanistic Insights into Chloride Ion Detection from the Atmospheric-Pressure Afterglow of an Argon Inductively Coupled Plasma

Journal:	*Journal of Analytical Atomic Spectrometry*
Manuscript ID	JA-ART-07-2018-000244.R1
Article Type:	Paper
Date Submitted by the Author:	28-Aug-2018
Complete List of Authors:	Lesniewski, Joseph; Georgetown University, Chemistry McMahon, William; Georgetown University, Chemistry Jorabchi, Kaveh; Georgetown University, Chemistry

Mechanistic Insights into Chloride Ion Detection from the Atmospheric-Pressure Afterglow of an Argon Inductively Coupled Plasma

Joseph E. Lesniewski, William P. McMahon, and Kaveh Jorabchi*

Department of Chemistry, Georgetown University, Washington, DC 20057, USA

* Corresponding author: kj256@georgetown.edu, phone: 2026872066

Abstract

Elemental analysis of chlorine using inductively coupled plasma mass spectrometry (ICP-MS) is challenging because of poor ion formation efficiency of Cl^+ in the argon plasma, and prevalence of isobaric interferences. To improve Cl detection, we have recently developed plasma assisted reaction chemical ionization (PARCI) in which an Ar-ICP is coupled to an atmospheric-pressure afterglow reaction tube, leading to high-sensitivity detection of Cl^-. We have shown that introduction of sodium and methanol into the ICP improves Cl^- sensitivity in PARCI-MS to levels better than those of conventional ICP-MS/MS. In this report, we probe the chloride ion formation mechanism in the ICP afterglow via examining the impact of the aerosol gas flow rate and torch box exhaust flow rate on Cl^- detection. Specifically, we evaluate analyte breakdown in the ICP, sampling of plasma products into the afterglow reaction tube, and ion-neutral reactions in the atmospheric-pressure afterglow as major processes for chloride ion formation in PARCI. We find that aerosol carrier gas flow rates ≤ 2.2 L/min result in compound-independent response factors for Cl, indicating sufficient residence time in the plasma for efficient breakdown of analytes. Notably, we show that torch box exhaust flow rate has a drastic impact on Cl^- sensitivity. This effect stems from its influence on plasma sampling efficiency and on ion-neutral reactions in the afterglow. Lastly, our results indicate that clusters formed in the afterglow reaction tube play critical roles in Cl^- detection. Specifically, $[NaClHCO_2]^-$ and $[NaClNO_2]^-$ are identified as key species for Cl^- detection from chlorinated compounds introduced into the ICP in conjunction with methanol and sodium. Ab-initio calculations indicate thermodynamically favorable reactions for formation of these cluster ions, supporting the importance of cluster formation in the ICP afterglow for high-sensitivity chloride ion detection.

1. Introduction

Inductively coupled plasma mass spectrometry (ICP-MS) is widely used for high-sensitivity elemental analysis. However, the capabilities of this technique are limited where analysis of low-mass and high-ionization-potential elements is needed. In particular, chlorine detection is hindered by low efficiency of Cl^+ formation in the argon plasma[1] and by polyatomic isobaric interferences such as $^{16}O^{18}OH^+$. Importantly, organochlorines have emerged as a prominent class of compounds with environmental and biological significance. For example, 23 of 28 chemicals adopted by the Stockholm Convention for global regulation are chlorinated.[2] Our examination of publicly available databases show that about 13% of the nearly 8000 drugs in the DrugBank[3] database contain chlorine, and 46% of the 768 compounds measured by the FDA's Pesticide Residue Monitoring Program[4] are chlorinated. Further, characterization of chlorine-containing water disinfection byproducts continues to be an active area of investigation.[5–7] Therefore, high-sensitivity elemental detection and isotopic analysis of chlorine is needed to help elucidate the environmental and biological impact of these compounds and their transformation products.

To address challenges in chlorine elemental analysis, instrumental techniques using ICP-high-resolution MS and ICP-MS/MS have emerged in recent years, focusing on reduction of isobaric interferences.[8–15] On the other hand, we have pursued improved ionization via development of plasma-assisted reaction chemical ionization (PARCI) as a chemical strategy to enhance sensitivity and to reduce isobaric interferences.[16–19] In particular, we recently reported a PARCI source using an argon ICP for detection of Cl^- ions from chlorinated compounds.[19] In the ICP-based PARCI, analyte aerosols are introduced into an ICP similar to a conventional ICP-MS. However, the plasma products in PARCI are sampled into an atmospheric-pressure reaction tube for post-plasma ion-neutral reactions. This is in contrast to the conventional ICP-MS where ions (plasma products) are sampled directly from the plasma into the first vacuum stage of the MS, and ion-neutral reactions during ion sampling are avoided.[19]

The post-plasma ion-neutral reactions in PARCI extend the ion formation pathways beyond thermal ionization in conventional ICP-MS, offering new chemical ionization strategies for elemental analysis.

Further, the reaction tube situated after the plasma lowers the plasma gas temperature, enabling detection of ions using readily available atmospheric-sampling mass spectrometers (e.g. LC-MS instruments). This alleviates the need for a dedicated elemental mass analyzer and expands the elemental MS capabilities such as negative ion detection currently unavailable in commercial ICP-MS instruments.

Importantly, we have demonstrated that ICP-based PARCI-MS offers higher sensitivity for chlorine (detected ions per second per ppb of Cl) via detection of Cl^- compared to that achieved via Cl^+ detection in ICP-MS/MS and ICP-high resolution MS.[8,12,19] Notably, we reported drastic sensitivity improvement in Cl^- detection using PARCI-MS upon concurrent introduction of sodium and methanol into the plasma.[19] We attributed this observation to chemical ionization effects in the afterglow, however, an exact mechanism of action for methanol and sodium remained to be investigated. In the current report, we characterize the impact of plasma and sampling operating parameters on Cl^- detection and offer insights into critical ion-neutral reactions in the plasma afterglow. These investigations provide insights into the effects of methanol and sodium and offer a roadmap for further improvements of PARCI by developing element-specific ionization strategies.

2. Experimental

2.1. PARCI

The ICP-based PARCI-MS setup used in this study has been described previously.[19] An updated diagram of the setup is shown in Figure S1 showing minor modifications to improve sensitivity and provide further control for experiments. Briefly, the analyte solution was introduced into a high efficiency nebulizer (HEN-120, Meinhard, Golden, CO) coupled to a cyclonic spray chamber (Twister Cyclonic P/N 20-809-0365, Glass Expansion, Pocasset, MA) using a 20-µL injection loop at a water flow rate of 200 µL/min supplied by an HPLC pump (SCL10AVP controller and LC10AD pump, Shimadzu, Columbia, MD). The nebulizer was operated at a constant gas flow rate of 1.25 standard liters per minute (SLPM) measured using a mass flow meter (Model 8270, Matheson, Montgomeryville, PA). The analyte aerosol was mixed with ionization reagent aerosol (200 µM sodium acetate in methanol) emerging from a second nebulizer (HEN-170, Meinhard, Golden, CO) and spray chamber (Twister Cyclonic P/N 20-809-0222, Glass Expansion, Pocasset, MA) operated at nebulizer gas flow rate of 0.55 SLPM (supplied by the internal mass flow controller of the ICP generator) and solution flow rate of 30 μL/min provided by a syringe pump (Model 100, KD Scientific, Holliston, MA). The mixed aerosol was directed into a tangential mixer (ML151008N, Meinhard, Golden, CO) where an argon makeup gas of varying flow rates (supplied by a mass flow controller, Model 946, MKS, Andover, MA) was added. This configuration allowed variation of total aerosol carrier gas flow rate with minimal impact on analyte and ionization reagent aerosol production and transport to the ICP. The plasma was sustained using a stand-alone ICP generator with a fully shielded torch box (NexION 2000, PerkinElmer Inc., Waltham, MA).

To control the torch box exhaust flow rate, a 4" inline fan (Model GLFANXINLINE4, iPower Inc., Industry, CA) was installed on the exhaust manifold of the torch box. The fan velocity was controlled by adjusting the input voltage using a variac (model Powerstat 3PN116B, ISE Inc., Cleveland, OH). An air velocity sensor (Model f661, Degree Controls Inc., Milford, NH) installed at the bottom air intake grid of the ICP torch box was used to monitor the exhaust flow.

An aluminum cylindrical interface provided plasma sampling for afterglow reactions. The interface provided a ¼" channel in its center terminating in a flat sampling orifice (2-mm i.d. and 1 mm thick). A stainless steel reaction tube with a ¼" o.d. and 0.19" i.d. was inserted into the channel. Compared to the previous report,[19] the reaction tube length was shortened to 50 mm and the tube was sealed to the interface using a graphite ferrule (Valco Instrument Co., Houston, TX) to minimize air diffusion into the post-plasma reaction region. The aluminum interface was threaded onto the water-cooled aluminum plate of the ICP generator. The plate was bolted to the front of the ICP torch box and the sampling orifice was aligned with the injector tube orifice. Operating parameters for PARCI are summarized in Table 1.

2.2. Mass spectrometers

A single quadrupole mass spectrometer (SQ 300, PerkinElmer Inc., Waltham, MA) was used for detection of ions emerging from the reaction tube. The electrospray ionization source from the instrument was removed and the PARCI source was placed such that the end of the reaction tube was aligned with the inlet of the MS and 5-10 mm away from the end plate. A nitrogen counterflow gas of 5 L/min at room temperature was used to limit the introduction of neutrals into the MS inlet. Negative ions were drawn into the inlet of the MS by applying potentials of +200 V to the end plate and +600 V to the glass capillary entrance. Background scans were collected in m/z range of 15 to 350 using 500 μs pulse counting time per point, 10 points per mass, and were averaged for 30 seconds. Both high declustering (-150 V capillary exit, -20 V skimmer) and low declustering (-30 V capillary exit, -20 V skimmer) conditions were used for background ion collections.

Cl sensitivity measurements were conducted in selected ion monitoring (SIM) mode at m/z values of 35 and 37 using high declustering potentials (see above) to convert all species to Cl^-. An integration time of 250 ms per ion was applied. Because of the high Cl background the ion optics were detuned to reduce the ion flux and to minimize premature aging of the detector. This was effected by setting the Q1 offset parameter to zero (normally it is set to +2 V), producing a suppression factor of 4.8 for both signal and background.

For ion identity confirmations, a time-of-flight MS (Axion, PerkinElmer Inc., Waltham, MA) was utilized. Because of the detector sensitivity to argon in this instrument, the PARCI source was placed off axis and a counterflow gas of 6.5 L/min was used to minimize argon introduction into the vacuum chamber. These settings compromised the sensitivity but the exact mass from the TOF provided confidence for the identification of the ions.

2.3. Argon gas velocity and temperature measurements

Argon gas flow measurements in the reaction tube were based on the velocity and the temperature of the gas emerging from the tube outlet. Temperature was measured using a thermocouple and velocity was measured by tracking the movement of water droplets entrained in the center of the argon flow emerging from the reaction tube. Details of these measurements are included in the electronic supplementary information.

2.4. Computational methods

Reaction thermochemistries were calculated at a theory level of ωB97xD/aug-cc-pVTZ using the approximate temperature at the end of the reaction tube in conditions where Cl sensitivity was optimized

(600K). This level of theory has been successfully used to describe the thermochemical properties of halide-neutral adducts.[20] Structures were first optimized using the MMFF94 force field in the Avogadro program[21] to generate initial geometries for each species. The geometries were then optimized at the final theory level using Gaussian 16.[22] In cases where more than one conformer was possible for a given ion or molecule, the lowest energy conformer was used. Gaussian output files for all molecules used in the calculation of the reaction energies are included in the electronic supplementary information.

2.5. Sample preparation and data analysis

Aqueous solutions of chloramphenicol and sodium chloride with 25 μM chlorine were used in experiments. Details of sample preparation and data analysis are included in the electronic supplementary information.

3. Results and discussion

To investigate Cl^- formation mechanism in PARCI, three major processes should be considered: 1) vaporization and breakdown of chlorinated analytes in the plasma, resulting in compound-independent response factors, 2) transfer of plasma products into the reaction tube, and 3) ion-neutral reactions of plasma products in the reaction tube. These processes are influenced by plasma operating parameters and plasma modifiers (e.g. sodium and organic solvents). Among the plasma operating parameters, aerosol gas flow rate and RF power exert the largest effects on the temperature and chemical composition of the sampling position in the plasma. Another important operating parameter is the torch box exhaust flow rate which influences the pressure in the torch box. Accordingly, flow of argon from the plasma into the reaction tube is reduced at increased exhaust flow rates. Note that this is in contrast to conventional ICP-MS where the effect of exhaust flow rate on plasma sampling is minimized because of the large pressure difference on the two sides of the sampler cone.

In the following sections, we examine the influence of aerosol carrier gas flow rate and exhaust flow rate on the three processes discussed above. We have used a constant RF power of 1100 W to limit the number of variables and to allow detailed exploration of the other parameters. This power level was selected based on good analytical performance for Cl^- detection in our previous investigations.[19] Moreover, all experiments utilized concurrent introduction of 200 μM methanolic sodium acetate into the plasma as ionization reagent (plasma modifier) to improve Cl^- sensitivity. For the evaluation of exhaust effects, the air velocity at the air intake grid of the torch box (see Experimental section) was used as an indicator for exhaust flow rate.

3.1. Analyte breakdown

Uniformity of chlorine response factors (detected ions per mole of chlorine in the sample) among different compounds offers insights into analyte vaporization and breakdown efficiency. We have selected chloramphenicol and sodium chloride as test analytes because they represent drastically different chemical properties for Cl. Figure 1 shows the impact of total aerosol carrier gas flow rate and exhaust velocity setting on the ratio of response factors between the two compounds. Ideally, one expects a response factor ratio of unity for compound-independent elemental ionization. Ratios of close to unity are observed at total carrier gas flow rates ≤ 2.2 SLPM. At higher flow rates, significant deviation from unity is observed, indicating extensive cooling of the central channel and compromised analyte vaporization and breakdown.[1,23]

Notably, the exhaust flow rate does not significantly influence response factor ratios in Figure 1 for aerosol flow rates ≤ 2.2 SLPM where compound-independent behaviors is observed. In contrast, the exhaust setting drastically impacts the reaction tube temperature as discussed in later sections. Accordingly, we infer that efficient analyte breakdown largely occurs in the plasma rather than in the reaction tube even at relatively high aerosol carrier gas flow rates used in our experiments compared to typical values of ~1 SLPM in conventional ICP-MS.

3.2. Sampling plasma products into the reaction tube

Analyte breakdown products are carried by the argon gas from the central channel of the plasma into the reaction tube. Therefore, the fraction of the gas flow from the central channel that enters the reaction tube reflects the sampling efficiency of the plasma products. The central channel gas flow is in turn largely composed of the aerosol carrier gas flow, especially at high carrier gas flow rates.[23,24]

Accordingly, one can estimate the sampling efficiency using the ratio of the argon flow rate in the reaction tube to total aerosol carrier gas flow rate. Note that flow rates in standard conditions must be used for the ratios to account for drastic changes in temperature between the gas introduced into the plasma and the gas in reaction tube.

To determine the argon flow rate in the reaction tube, the gas velocity (v) and the temperature of the gas at the tube outlet were monitored as discussed in the Experimental section. Assuming a laminar flow with a parabolic profile for an ideal gas, the standard (273 K, and 1 atmosphere) volumetric gas flow rate (F_v) is calculated using Equation 1:

$$F_v = \frac{\pi r^2 v}{2} \times \frac{273}{T} \times \frac{P}{1} \qquad (1)$$

where r is the inner radius of the reaction tube, T is the gas temperature at the tube end, and P is the lab pressure in atmospheres. The factor 2 in the denominator arises from the relationship between average gas velocity and the maximum velocity measured at the center of a laminar flow profile. The sampling efficiency is then calculated by F_v/F_t where F_t is the total carrier gas flow rate in standard liters per minute (SLPM) supplied by mass flow meters in the sample introduction.

Figures 2a and 2b show the effects of the total aerosol carrier gas and exhaust flow rates on the gas temperature and gas velocity at the reaction tube outlet. Figure 2a depicts that the reaction tube gas temperature generally increases with increasing carrier gas flow rate and decreasing exhaust flow rate, illustrated by the diagonal trend from the upper left corner to the bottom right corner of Figure 2a. At lower exhaust flow rates a larger flow of argon from the plasma is directed into the reaction tube. This provides a greater flow of thermal energy into the tube, causing higher temperatures in the reaction tube. The effect of aerosol carrier gas is determined by two opposing factors. As the aerosol gas flow rate increases, so does the amount of hot argon gas entering the reaction tube (see the sampling efficiency discussion below). This results in an increase in the reaction tube gas temperature. However, higher aerosol gas flow rate also leads to plasma cooling, counteracting the effect of greater fluid flow rate entering the tube. The increasing reaction tube temperatures with aerosol gas flow rates up to 2.4 SLPM in Figure 2a suggest that the greater fluid flow into the tube is the dominant factor in this operating range. Interestingly, the tube outlet gas temperature decreases at carrier gas flow rates > 2.4 SLPM for all exhaust settings. This indicates significant plasma cooling to the extent that the larger flow of argon into the tube does not compensate for the loss of thermal energy due to plasma cooling. This observation is also in agreement with deviations from compound-independent response factors at aerosol gas flow rates > 2.4 SLPM in Figure 1, further confirming the excessive plasma cooling at high aerosol flow rates that compromises analyte breakdown. Figure 2b illustrates that the reaction tube gas velocity also increases in a diagonal manner similar to tube gas temperature. However, the impact of the exhaust flow rate on gas velocity is minimized as the carrier gas flow rate is increased, evident from near vertical contour lines at aerosol carrier gas flow rates > 2.4 SLPM in Figure 2b.

Figure 2c depicts the sampling efficiencies calculated from the data in Figures 2a and 2b using Equation 1. An increase in plasma sampling efficiency is observed with increasing aerosol gas flow rate and decreasing exhaust flow rate (diagonal trend) similar to Figures 2a and 2b. The effect of exhaust velocity is minimized at aerosol gas flow rates > 2.4 SLPM, indicating the dominance of carrier gas flow rate in determining plasma sampling efficiency at high aerosol flow rates. Note that such high flow rates do not produce compound-independent response (Figure 1), thus are less desirable for quantitative elemental analysis. Interestingly, the sampling efficiencies are lower than 50% within the analytically preferred region for elemental quantification (aerosol gas flow rate < 2.4 SLPM) in Figure 2c, indicating that sensitivity improvements could be made by modification of the interface to sample a larger fraction of the central channel gas flow.

3.3. Effect of chemical reactions

With the insights gained above for the impact of operating parameters on analyte breakdown and plasma sampling efficiencies, we now focus on evaluating effects of chemical reactions on Cl^- sensitivity. To this end, we examined the effect of aerosol carrier gas flow and exhaust flow rates on Cl^- sensitivities in operating conditions similar to those in Figures 2a-2c. The results are shown in Figure 2d as a contour map for flow injection peak areas of a 12.5 μM chloramphenicol sample (25 μM Cl).

Figure 2d illustrates that the highest Cl^- sensitivity is observed at total carrier gas flow rate of 2.0 SLPM and an exhaust velocity of 5.8 m/s. We expect near-complete vaporization and breakdown of analytes in these optimum operating conditions based on the compound-independent response shown in Figure 1. However, the trends for sensitivity in Figure 2d do not coincide well with trends for plasma sampling efficiency (Figure 2c) within the analytically preferred region for quantitative elemental analysis (aerosol gas flow rate < 2.4 SLPM). In other words, plasma operating conditions that increase sampling efficiency do not necessarily lead to improved ion detection efficiencies, and the optimum ion signal is observed at a plasma sampling efficiency of only 26%. This observation highlights the major influence of complex chemical reactions on detected Cl^- signals as discussed below.

Consider the operating conditions of 1.8 SLPM total carrier gas flow rate and exhaust velocity of 3.8 m/s (bottom left corner in Figure 2c). The sampling efficiency into the reaction tube in these conditions (28%) is similar to that of the optimum operating conditions for Cl^- sensitivity (26% at 2.0 SLPM carrier flow rate and 5.8 m/s exhaust velocity). Further, both reaction tube gas temperature and gas velocity in Figures 2a and 2b are similar between the bottom left corner and the optimum operating conditions. Therefore, species sampled into the reaction tube are likely to experience equivalent residence time and reaction temperature in the afterglow between the two conditions. Nevertheless, sensitivity in the bottom left corner of Figure 2d is 55 times lower than that at the optimum operating conditions. Such a drastic difference in sensitivity with similar plasma sampling and afterglow reaction conditions indicates a drastic change in the chemical nature of the species sampled into the reaction tube between the two conditions. The chemical transformations of the analytes in the plasma prior to sampling into the reaction tube is controlled by aerosol residence time within the plasma which in turn is a function of aerosol gas flow rate. Therefore, variations in chemical composition of the plasma sampling point at different aerosol gas flow rates are expected. However, one must note that in-plasma reactions of the analytes at high aerosol gas flow rates in our experiments are likely more complex than mere atomization, and are likely to involve formation of polyatomic species as discussed later in this report.

Now consider a total carrier gas flow rate of 2.0 SLPM (optimum value for Cl sensitivity) at various exhaust velocities in Figure 2. In these conditions, the in-plasma reactions are set by the carrier gas flow rate and are expected to be independent of the exhaust flow rate. This expectation is further supported by the minimal impact of the exhaust flow rate on the response factor ratios in Figure 1 at aerosol gas flow rate of 2.0 SLPM. Figure 2c shows that at constant carrier gas flow rate of 2.0 SLPM, the sampling efficiency increases slightly as the exhaust velocity is reduced from the optimum value of 5.8 m/s to 3.8 m/s. In contrast, the sensitivity is reduced by fivefold as depicted in Figure 2d. Notably, both velocity and temperature of the gas in the reaction tube increase as the exhaust velocity is reduced (Figures 2a and 2b). Therefore, the sampled species from the plasma spend less time in the reaction tube and the post-plasma reactions occur at a higher temperature. These results suggest that reactions in the tube also play a critical role in the ionization of Cl in addition to the in-plasma reactions controlled by the total carrier gas flow.

In summary, the results indicate that both in-plasma and post-plasma reactions play critical roles in Cl^- detection. To gain insight into these reactions, we have explored the background ions and their relation to Cl^-.

3.3.1. Background ions

In our previous work on Cl^- detection using ICP-based PARCI,[19] four major background ions were identified as NO_2^-, CN^-, OCN^-, and HCO_2^- upon introduction of methanolic sodium acetate into the plasma. Among these ions, HCO_2^- was specific to methanol introduction, suggesting that NO_2^-, CN^-, OCN^- are mainly a result of nitrogen diffusion into the plasma and afterglow while the formate ion is a product of methanol introduction. Importantly, we observed a loose correlation between Cl^- sensitivity and HCO_2^- intensity, indicating a potential mechanistic relation. These experiments, however, were conducted at high declustering potentials (nozzle-skimmer potential difference of 130 V) to improve Cl^- ion detection. Such ion transmission conditions lead to loss of easily fragmentable species, hampering a comprehensive insight into the chemical composition of the ionization environment. In the current report, we collected spectra using low declustering potentials achieved at a nozzle-skimmer potential difference of 10 V to further the insights into ionization reactions.

Figure 3 compares the background spectra with high and low declustering potentials at optimum plasma operating conditions for Cl^- detection. It is clear that high-mass ions observed by soft ion transmission (low declustering) are fragmented in harsh ion transmission conditions. Notably, $[Na(HCO_2)_2]^-$, $[NaHCO_2NO_2]^-$ and $[NaHCO_2OCN]^-$ are the most prominent ions in the spectrum of Figure 3 with soft ion transmission. Molecular formulas of these clusters were further confirmed by exact mass measurements using a time-of- flight mass spectrometer with mass accuracy better than 5 ppm.

The presence and relative intensities of clusters in Figure 3 suggest the existence of $NaHCO_2$ as a major species in the reaction tube to form first order clusters ($[Na(HCO_2)_2]^-$, $[NaHCO_2NO_2]^-$ and $[NaHCO_2OCN]^-$) via adduction to HCO_2^-, NO_2^-, and OCN^- as shown in thermodynamically favorable Reactions 1-3 in Table 2. Higher cluster orders ($[Na_n(HCO_2)_{n+1}]^-$, $[Na_n(HCO_2)_nNO_2]^-$, and $[Na_n(HCO_2)_nOCN]^-$, with $n > 1$) are formed by the stepwise reaction of sodium formate with the first order clusters. Note that the gas temperature in the tube is reduced during the transfer of species from the plasma toward the mass spectrometer. Calculations in Table 2 are conducted at a temperature of 600 K, representing the tube outlet temperature at optimum operating conditions.

3.3.2. Relation of background ions to Cl^-

To identify the background ions relevant to Cl^- detection, we measured the background spectra using soft ion transmission (low declustering) at a range of exhaust and carrier flow rates identical to those in Figure 2. We then correlated the results with the Cl^- sensitivities of Figure 2d by linear regression of (x,y) points where x is the measured background ion intensity and y is the Cl^- sensitivity at each operating condition. All background ions in the mass range 15-350 that showed intensities ≥ 100,000 cps in at least one operating condition were considered. Figure S2 shows the r^2 of the regressions as a function of the ion m/z. No strong correlation was observed based on absolute ion intensities. However, when the ion intensities were normalized to the total ion count (TIC) in each spectrum, strong correlations with Cl^- sensitivity were observed for m/z 113 ($r^2 = 0.95$) and 114 ($r^2 = 0.86$) as shown in Figure 4. These m/z values correspond to $[Na(HCO_2)_2]^-$ and $[NaHCO_2NO_2]^-$ ions. Note that the carbon isotope contribution to m/z 114 from m/z 113 is minimal compared to the contribution from $[NaHCO_2NO_2]^-$ as evident from the relative intensities of the two ions in Figure 3. Therefore, no isotopic correction is considered in this analysis. The correlations create a link between formate, nitrite, sodium and chloride and offer an avenue to explore the mechanistic role of sodium and methanol introduced into the plasma for enhanced Cl^- detection.

Figure 5 depicts contour maps of TIC-normalized and absolute background ion intensities for nitrite, formate and their corresponding cluster ions. A clear visual similarity exists between $[Na(HCO_2)_2]^-$ TIC-normalized intensity map in Figure 5b and Cl^- sensitivity in Figure 2d (both having maximum values at aerosol gas flow = 2.0 SLPM and exhaust velocity of 5.8 m/s) while a lower degree of similarity is observed between $[NaHCO_2NO_2]^-$ TIC-normalized intensity map (Figure 5f) and Cl^-. These visual correlations are consistent with the results of regression analyses in Figure 4. Further, the maps for absolute ion intensities in Figure 5 do not show similarities to the map of Cl^- sensitivity consistent with regressions in Figure S2.

The TIC-normalized values quantify the prominence of the ions within the spectra and reflect the importance of a particular ionization pathway relative to other reactions. For example, $[Na(HCO_2)_2]^-$ and $[NaHCO_2NO_2]^-$ show their highest absolute intensities at an exhaust setting of 3.8 m/s and carrier gas flow rate of 2.4 SLPM in Figures 5j and 5n. However, the Cl^- sensitivity in these conditions is 2.7 times lower than that at the optimum operating conditions (Figure 2d). In contrast, TIC-normalized intensities for $[Na(HCO_2)_2]^-$ and $[NaHCO_2NO_2]^-$ are reduced by factors of 2 and 2.4 at exhaust setting of 3.8 m/s and carrier gas flow rate of 2.4 SLPM compared to the optimum operating conditions (Figures 5b and 5f). The reduced TIC-normalized intensities indicate increased contribution of other ionization reactions relative to the first-order cluster formation. Two examples of such reactions are revealed upon examination of the background spectrum at exhaust setting of 3.8 m/s and carrier gas flow rate of 2.4 SLPM shown in Figure S3: 1) new prominent ions compared to Figure 3 such as $[(HCO_2H)NO_2]^-$, $[(HCO_2H)HCO_2]^-$, $[(HCO_2H)OCN]^-$, $[Na(HCO_2)_2(HCO_2H)]^-$, and $[Na(HCO_2)NO_2(HCO_2H)]^-$ indicate presence of formic acid (HCO_2H) and clustering of ions with this neutral as a major ionization pathway, and 2) enhanced intensities of second order clusters ($[Na_2(HCO_2)_3]^-$ and $[Na_2(HCO_2)_2NO_2]^-$) relative to first-order clusters ($[Na(HCO_2)_2]^-$ and $[Na(HCO_2)NO_2]^-$) highlight a shift in cluster size distribution toward higher orders compared to the optimum conditions shown in Figure 3. This indicates promoted clustering with $NaHCO_2$.

In summary, best Cl^- sensitivities are observed in conditions that not only produce high intensities for $[Na(HCO_2)_2]^-$ and $[Na(HCO_2)NO_2]^-$ but also ensure the favorable formation of theses first-order clusters over other reactions.

3.3.3. Effect of exhaust flow and carrier gas flow rates on clustering

The changes in cluster size distribution for $[Na_n(HCO_2)_{n+1}]^-$ and $[Na_n(HCO_2)_nNO_2]^-$ offer insights into the impact of exhaust and carrier gas flow rates on clustering reactions. To examine these effects, we investigated the impact of operating parameters on average cluster order (*A*) for each family of cluster ions defined by Equations 2 and 3:

$$A_{HCO_2^-} = \frac{\sum_{n=0}^{3} n \times I_{\ [Na_n(HCO_2)_{n+1}]^-}}{\sum_{n=0}^{3} I_{\ [Na_n(HCO_2)_{n+1}]^-}} \qquad (2)$$

$$A_{NO_2^-} = \frac{\sum_{n=0}^{3} n \times I_{[Na_n(HCO_2)_nNO_2]^-}}{\sum_{n=0}^{3} I_{[Na_n(HCO_2)_nNO_2]^-}} \qquad (3)$$

Figure 6 depicts the contour maps of the average cluster order. Note that the values at the aerosol gas flow rate of 1.8 SLPM in Figure 6 should be treated with caution because of the large uncertainties caused by low ion intensities at these operating parameters (see Figures 5i-p).

Figures 6a and 6b demonstrate that average cluster order increases with increasing exhaust setting at a constant aerosol gas flow rate of 2.0 SLPM (optimum for Cl^- detection). This is in agreement with the trends in Figures 2a and 2b where reaction tube gas temperature and gas velocity are reduced with increasing exhaust flow at aerosol gas flow rate of 2.0 SLPM. Lower temperatures and longer residence times in the ICP afterglow promote clustering and shift the cluster order distribution to higher orders. Interestingly, the change in average cluster order as a function of the exhaust flow is minimized at higher aerosol gas flow rates. This trend is also in agreement with Figures 2a and 2b where the effect of exhaust flow on gas temperature and gas velocity are reduced at high aerosol gas flow rates.

Figures 6a and 6b also depict that the average cluster size generally increases as the aerosol gas flow rate is increased from the optimum value of 2.0 SLPM. This result is intriguing at first because one expects a lower clustering extent based on higher gas temperature and gas velocity within the reaction tube, evident from Figures 2a and 2b for increasing aerosol gas flow rates. However, it must be noted that plasma conditions, upstream of the reaction tube are also impacted by higher carrier gas flow rates. Specifically, increased carrier gas flow rates reduce the residence time of aerosol in the plasma and decrease the temperature of the central channel. In-plasma reactions in such operating conditions are expected to promote the formation of polyatomic species, like $NaHCO_2$. The ensuing increase in the concentration of $NaHCO_2$ within the reaction tube could ultimately shift the clustering reactions (Reactions 1-3, Table 2) to the right, compensating for the opposite effects of higher temperature and shorter afterglow reaction times.

3.3.4. Implications for Cl ionization

To elucidate the relationship between the prominence of $[Na(HCO_2)_2]^-$ and $[Na(HCO_2)NO_2]^-$ clusters in the spectra and chloride ion detection, we examined the possibility of detecting similar Cl-containing clusters. Accordingly, we monitored ions at m/z values corresponding to Cl^-, $[NaHCO_2Cl]^-$, $[NaNO_2Cl]^-$, $[Na_2(HCO_2)_2Cl]^-$, and $[Na_2HCO_2NO_2Cl]^-$ using SIM mode upon flow injections of chloramphenicol into the plasma with aerosol gas flow rate of 2.0 SLPM, exhaust velocity of 5.8 m/s and RF power of 1100 W. These conditions correspond to the highest signal for Cl^- (Figure 2d). However, unlike the experiments for Figure 2d, we utilized a low declustering potential (10 V) to preserve the clusters.

Figure 7 shows relative intensities for the expected species, confirming their formation. Notably, the distribution of Cl-containing species in Figure 7 resembles those of $[Na_n(HCO_2)_{n+1}]^-$ and $[Na_n(HCO_2)_nNO_2]^-$ clusters (See Figure 3) where the first-order clusters are the dominant species. The larger abundance of the Cl-containing clusters in Figure 7 relative to the un-clustered Cl^- suggests that the

Cl^- ions detected in harsh ion transmission (e.g. in Figure 2d) are largely a result of cluster ion breakdown upon ion activation in the nozzle-skimmer area.

The calculated thermochemistries in Table 2 can be used to evaluate the competitive fragmentation pathways upon activation of the cluster ions. For example $[Na_2(HCO_2)_2Cl]^-$ and $[Na_2HCO_2NO_2Cl]^-$ may release Cl^-, HCO_2^-, and NO_2^- upon activation. Thermochemistries for Reactions 4-7 in Table 2 show that the release of Cl^- from the first-order clusters requires less energy compared to that needed for release of NO_2^- and HCO_2^-. Therefore, Cl^- is predicted to be the major fragmentation product of the clusters.

Experimental investigation of the fragmentation products require MS/MS experiments. Coupling PARCI to an MS/MS instrument is currently under development in our laboratory. Fortunately, similar clusters can be generated using electrospray ionization from a solution of sodium chloride and sodium formate as shown in Figure S4a, obtained using an ESI-triple quadrupole MS instrument. Figure S4b depicts that activation of $[Na(HCO_2)Cl]^-$ at a collision energy (CE) of 12 eV mainly produces Cl^- as predicted above. Release of HCO_2^- becomes competitive at higher activation energies (CE = 20 eV, Figure S4c) where fragmentation channels with higher activation barriers are accessed.

Importantly, the cluster order (n) has a major influence on the efficiency of Cl^- release from $[Na_n(HCO_2)_nCl]^-$ and $[Na_n(HCO_2)_{n-1}NO_2Cl]^-$ clusters. As the cluster order grows, more fragmentation pathways become available, competing for the energy deposited in the ion during activation. This is shown in Figures S4d and S4e for fragmentation of $[Na_2(HCO_2)_2Cl]^-$ and $[Na_3(HCO_2)_3Cl]^-$ at CE = 20 eV, demonstrating that lower order clusters become the major fragmentation products via loss of $NaHCO_2$. The reduced fragmentation efficiency to Cl^- for cluster orders $(n) > 1$ is in agreement with the lower Cl^- sensitivity observed at operating conditions that promote clustering beyond the first-order clusters.

3.3.5. Mechanistic considerations for enhancement of Cl^- detection by first-order clusters

To understand the role of methanol (responsible for formate generation) and sodium in improving Cl^- detection from ICP afterglow, we now consider two ionization mechanisms that involve formation of first order clusters. In the first mechanism, Cl^- ions form in the plasma or in the afterglow via electron capture reactions and react with plasma generated neutrals in the reaction tube to create the chlorinated clusters. Reactions 4 and 5 in Table 2 indicate favorable thermochemistry for clustering reactions of Cl^-. In this mechanism, improvements in Cl^- detection upon introduction of sodium and methanol could be explained by preventing Cl^- loss upon clustering. One possibility for a Cl^- loss mechanism is ion-ion recombination in the afterglow. Clusters will have lower mobilities compared to the Cl^- ion, reducing the ion-ion recombination rate.

The second mechanism is formation of NaCl and subsequent ion-neutral reactions. One can consider sodium transfer reactions of NaCl with formate and nitrite, leading to release of Cl^- as shown by Reactions 8 and 9 in Table 2. Subsequently, the released Cl^- could undergo clustering reactions as discussed above. Alternatively, clusters can form via adduction of formate and nitrite to NaCl (Reactions 6 and 7), or via formate and nitrite transfer from first order clusters of these ions (Reactions 10-12) in Table 2. Given the prominence of the first order clusters for formate and nitrite in our optimum experimental conditions for Cl^- sensitivity (Figure 3), the formate and nitrite ions are likely to react rapidly with sodium formate, depleting the population of these ions in the reactive flow. Accordingly, we infer that the nitrite and formate transfer reactions (Reactions 10-12 in Table 2) would play significant roles in formation of $[NaHCO_2Cl]^-$ and $[NaNO_2Cl]^-$ among the Reactions 6-12 which consider NaCl as an intermediate species in ionization of chlorine.

The major difference between the first and second mechanism is that the first one starts with a Cl^- ion and solely relies on loss prevention to explain sensitivity improvements by clustering, while the second one considers formation of NaCl and subsequent ionization of this neutral as an ionization route to improve formation of Cl^- ions. Elucidation of relative importance between the two mechanisms would require further investigations, however, both mechanisms clearly indicate the importance of cluster formation in improving Cl^- detection in the ICP afterglow.

3.3.6. Application to fluorine detection

In an effort to evaluate the effectiveness of above ionization reactions for analysis of fluorine, we investigated detection of fluoride ion and its clusters. Early studies in negative mode ICP-MS have revealed that Cl^- and F^- ions are observed with similar sensitivities as a result of complete atomization in the plasma and subsequent electron capture by the atoms.[25–28] In our experimental investigations, however, we have not been able to observe fluoride or fluorine-containing clusters upon injection of 500 μM para-fluoro-phenylalanine while chlorine clusters are readily observed by injections of 10 μM chloramphenicol and 20 μM NaCl. This observation is consistent with both mechanisms discussed above. F^- has a large sodium ion affinity and can readily undergo sodium ion transfer reaction with sodium formate and sodium nitrite forming NaF (Reactions 13 and 14). Accordingly, both mechanisms predict NaF as a plasma product for fluorinated compounds. The adduction of nitrite and formate to NaF is favorable (Reactions 15 and 16) and can be an ionization route for cluster formation. However, formate and nitrite ions are rapidly depleted via adduction to $NaHCO_2$ in our experimental conditions as discussed above, making the formate and nitrite transfer reactions (17, 18, 19) dominant ion formation pathways. Importantly, the thermochemistries indicate that the anion transfer to NaF is not as favorable as that for NaCl, likely resulting in establishment of equilibrium for these reactions. Moreover, high concentration of $NaHCO_2$ would push the equilibrium left in reactions 17-19, further reducing ionization efficiency. In summary, the ionization mechanisms discussed above are consistent with the experimental observations for both F and Cl, offering support for the explanation of chloride ion enhancement in the presence of methanol and sodium, while fluorine detection as a negative ion is hindered in similar experimental conditions.

4. **Conclusions**

We have examined the major chloride ion formation steps for elemental analysis of chlorine using an Ar-ICP with an atmospheric afterglow reaction region. This configuration is an implementation of a general approach described as plasma-assisted reaction chemical ionization. Our results indicate that aerosol gas flow rates ≤ 2.2 SLPM using a 1.5-mm i.d. injector and 1100 W RF power provide sufficient breakdown of analytes for compound-independent Cl response. Unlike conventional ICP-MS, the exhaust flow rate plays a critical role in high-sensitivity detection of Cl in plasma-assisted reaction chemical ionization. The effect of exhaust is two-fold: 1) it controls the sampling efficiency of plasma products into the reaction tube, and 2) it affects the temperature and velocity of the gas in the reaction tube, in turn impacting ionization reactions. The gas flow measurements in the tube reveal that sampling efficiencies of ~26% are achieved at optimum operating conditions for best Cl^- sensitivity, indicating that sensitivity enhancements could be achieved by improved reaction interface designs with higher plasma sampling efficiencies.

Importantly, key observations have revealed cluster formation as a critical process for detection of Cl^- using methanolic sodium acetate as an ionization reagent in PARCI. These observations include: 1) strong correlation between Cl^- sensitivities (measured at high declustering potentials) and TIC-normalized intensities of $[Na(HCO_2)_2]^-$ and $[NaHCO_2NO_2]^-$ detected with soft ion sampling, and 2) observation of $[NaHCO_2Cl]^-$ and $[NaNO_2Cl]^-$ as dominant chlorine-containing ions detected with soft ion sampling (low declustering potential) upon injection of chlorinated analytes. These observations indicate that the improved Cl^- detection at high declustreing potentials is likely a result of cluster fragmentation and release of Cl^- from various clusters upon ion activation in the nozzle-skimmer area of the MS. The formation of clusters is influenced by the aerosol carrier gas flow rate, which determines the in-plasma reaction conditions as well as the gas temperature and velocity in the reaction tube. Similarly, the torch box exhaust setting affects the cluster formation via its influence on reaction tube gas temperature and gas velocity (reaction time).

The chlorine-containing clusters may be a result of chloride ion formation and subsequent adduction to plasma generated neutrals (such as $NaHCO_2$), preventing chloride ion loss via ion-ion recombination reactions. Alternatively, the clusters may be generated via formation of NaCl and transfer of formate and nitrite from first order clusters of these ions. Both mechanisms are viable as indicated by ab-initio calculations, and offer an explanation for improved Cl^- detection via concurrent introduction of sodium and methanol into the plasma. Note that formate is a product of methanol introduction. Both mechanisms are also consistent with the low sensitivity of fluorine detection in negative mode PARCI-MS.

Our studies indicate that effective atmospheric-pressure ion-molecule reactions can be utilized to increase sensitivity of elemental ionization for chlorine. In particular, the insights gained in these studies provide the grounds for designing a more sensitive ion source for detection of Cl and F. Importantly, implementation of the afterglow reactions also creates a low-temperature buffer between the extremely hot ICP and the mass spectrometer. Accordingly, a wide range of commercially available atmospheric-sampling mass spectrometers with high-resolution and MS/MS capabilities could be used for PARCI-MS to improve analytical performance.

Conflict of interest

Kaveh Jorabchi is an inventor of plasma assisted reaction chemical ionization (PARCI) patented under US patent #9,966,243.

Acknowledgements

This material is based upon work supported by the National Science Foundation (NSF) under CHE-1507304. We thank PerkinElmer Inc. for the loan of the single quadrupole and time of flight mass spectrometers and the ICP generator used in these studies. We are grateful to Dr. Hamid Badiei of PerkinElmer for constructive discussions during the course of this research.

References

1 H. Niu and R. S. Houk, *Spectrochim. Acta Part B At. Spectrosc.*, 1996, **51**, 779–815.

2 Secretariat of the Stockholm Convention, The Stockholm Convention on Persistent Organic Pollutants, http://chm.pops.int/, (accessed 7 July 2018).

3 D. S. Wishart, Y. D. Feunang, A. C. Guo, E. J. Lo, A. Marcu, J. R. Grant, T. Sajed, D. Johnson, C. Li, Z. Sayeeda, N. Assempour, I. Iynkkaran, Y. Liu, A. Maciejewski, N. Gale, A. Wilson, L. Chin, R. Cummings, D. Le, A. Pon, C. Knox and M. Wilson, *Nucleic Acids Res.*, 2018, **46**, D1074–D1082.

4 US Food & Drug Administration, Pesticide Residue Monitoring Program, https://www.fda.gov/Food/FoodborneIllnessContaminants/Pesticides/ucm582707.htm, (accessed 7 July 2018).

5 E. E. Lavonen, M. Gonsior, L. J. Tranvik, P. Schmitt-Kopplin and S. J. Köhler, *Environ. Sci. Technol.*, 2013, **47**, 2264–2271.

6 C. K. Remucal and D. Manley, *Environ. Sci. Water Res. Technol.*, 2016, **2**, 565–579.

7 A. Kinani, H. Salhi, S. Bouchonnet and S. Kinani, *J. Chromatogr. A*, 2018, **1539**, 41–52.

8 B. Klencsár, E. Bolea-Fernandez, M. R. Flórez, L. Balcaen, F. Cuyckens, F. Lynen and F. Vanhaecke, *J. Pharm. Biomed. Anal.*, 2016, **124**, 112–119.

9 B. Klencsár, L. Balcaen, F. Cuyckens, F. Lynen and F. Vanhaecke, *Anal. Chim. Acta*, 2017, **974**, 43–53.

10 J. T. P. Barbosa, C. M. M. Santos, L. dos S. Bispo, F. H. Lyra, J. M. David, M. das G. A. Korn and E. M. M. Flores, *Food Anal. Methods*, 2013, **6**, 1065–1070.

11 J. Nelson, H. Hopfer, F. Silva, S. Wilbur, J. Chen, K. Shiota Ozawa and P. L. Wylie, *J. Agric. Food Chem.*, 2015, **63**, 4478–4483.

12 X. Bu, T. Wang and G. Hall, *J. Anal. At. Spectrom.*, 2003, **18**, 1443–1451.

13 J. S. de Gois, M. Costas-Rodríguez, P. Vallelonga, D. L. G. Borges and F. Vanhaecke, *J. Anal. At. Spectrom.*, 2016, **31**, 537–542.

14 J. Renpenning, A. Horst, M. Schmidt and M. Gehre, *J. Anal. At. Spectrom.*, 2018, **33**, 314–321.

15 M. Ohata and A. Wada, *Anal. Methods*, 2017, **9**, 4004–4010.

16 H. Wang, N. Lin, K. Kahen, H. Badiei and K. Jorabchi, *J. Am. Soc. Mass Spectrom.*, 2014, **25**, 692–695.

17 H. Wang, C. S. Minardi, H. Badiei, K. Kahen and K. Jorabchi, *Analyst*, 2015, **140**, 8177–8185.

18 N. Lin, H. Wang, K. Kahen, H. Badiei and K. Jorabchi, *Anal. Chem.*, 2014, **86**, 7954–7961.

19 J. E. Lesniewski, W. P. McMahon, K. Zheng, H. Wang, H. Badiei and K. Jorabchi, *J. Anal. At. Spectrom.*, 2017, **32**, 1757–1765.

20 N. Hyttinen, R. V. Otkjær, S. Iyer, H. G. Kjaergaard, M. P. Rissanen, P. O. Wennberg and T. Kurtén, *J. Phys. Chem. A*, 2018, **122**, 269–279.

21 M. D. Hanwell, D. E. Curtis, D. C. Lonie, T. Vandermeersch, E. Zurek and G. R. Hutchison, *J. Cheminformatics*, 2012, **4**, 17.

22 M. J. Frisch, G. W. Trucks, H. B. Schlegel, G. E. Scuseria, M. A. Robb, J. R. Cheeseman, G. Scalmani, V. Barone, G. A. Petersson, H. Nakatsuji, X. Li, M. Caricato, A. V. Marenich, J. Bloino, B. G. Janesko, R. Gomperts, B. Mennucci, H. P. Hratchian, J. V. Ortiz, A. F. Izmaylov, J. L. Sonnenberg, Williams, F. Ding, F. Lipparini, F. Egidi, J. Goings, B. Peng, A. Petrone, T. Henderson, D. Ranasinghe, V. G. Zakrzewski, J. Gao, N. Rega, G. Zheng, W. Liang, M. Hada, M. Ehara, K. Toyota, R. Fukuda, J. Hasegawa, M. Ishida, T. Nakajima, Y. Honda, O. Kitao, H. Nakai, T. Vreven, K. Throssell, J. A. Montgomery Jr., J. E. Peralta, F. Ogliaro, M. J. Bearpark, J. J. Heyd, E. N. Brothers, K. N. Kudin, V. N. Staroverov, T. A. Keith, R. Kobayashi, J. Normand, K. Raghavachari, A. P. Rendell, J. C. Burant, S. S. Iyengar, J. Tomasi, M. Cossi, J. M. Millam, M. Klene, C. Adamo, R. Cammi, J. W. Ochterski, R. L. Martin, K. Morokuma, O. Farkas, J. B. Foresman and D. J. Fox, *Gaussian 16 Rev. B.01*, Wallingford, CT, 2016.

23 H. Lindner, A. Murtazin, S. Groh, K. Niemax and A. Bogaerts, *Anal. Chem.*, 2011, **83**, 9260–9266.

24 H. Lindner and A. Bogaerts, *Spectrochim. Acta Part B At. Spectrosc.*, 2011, **66**, 421–431.

25 J. E. Fulford and E. S. K. Quan, *Appl. Spectrosc.*, 1988, **42**, 425–428.

26 G. H. Vickers, D. A. Wilson and G. M. Hieftje, *Anal. Chem.*, 1988, **60**, 1808–1812.

27 M. Chtaib and J.-P. Schmit, *J. Anal. At. Spectrom.*, 1988, **3**, 315–318.

28 A. A. Pupyshev and V. T. Surikov, *Spectrochim. Acta Part B At. Spectrosc.*, 2004, **59**, 1021–1031.

Figure Captions

Figure 1. Ratio of Cl response factors from flow injections of NaCl and chloramphenicol as a function of carrier gas flow rate at various exhaust velocity settings. Error bars reflect one standard deviation of the average based on triplicate injections of each compound.

Figure 2. Effect of aerosol carrier gas flow rate and exhaust flow rate at 1100 W on a) temperature at reaction tube outlet, b) argon gas velocity flowing out of the reaction tube, c) sampling efficiency into the reaction tube calculated from the ratio of measured gas flow rate at the end of the reaction tube (Equation 1) to the total aerosol carrier gas flow rate, and d) Cl^- sensitivity measured as the average peak area from triplicate injections of 12.5 μM chloramphenicol. Contour plots are utilized to facilitate identification of trends using Delaunay triangulation and linear interpolation between the data points to color the contours. Experimental values are indicated at the grid points. A nozzle-skimmer potential difference of 130 V was used in experiments of Figure 2d to improve Cl^- detection sensitivity.

Figure 3. Effect of declustering potential on background ions at optimized ion source operating conditions for best Cl^- sensitivity (2.0 SLPM carrier flow rate, 5.8 m/s exhaust velocity, 1100 W RF power). The inset shows enlarged mass spectrum for the section with m/z > 170. Methanolic sodium acetate was used as ionization reagent. High declustering refers to 130 V potential difference between nozzle and skimmer of the MS while low declustering refers to 10 V potential difference.

Figure 4. a) r^2 values for linear regression of background ions' normalized intensities (collected at low declustering nozzle-skimmer potential) with $^{35}Cl^-$ sensitivity (measured at high declustering potential) at carrier gas flow and exhaust flow rates identical to those in Figure 2. b) Correlation plots of normalized intensities for m/z 113 ($[Na(HCO_2)_2]^-$), and c) m/z 114 ($[NaHCO_2NO_2]^-$). The background ion intensities were normalized to the total ion counts in each spectrum.

Figure 5. a-h) TIC-normalized and, i-p) absolute intensities of formate and nitrite ions and their clusters with sodium formate as a function of carrier gas flow rate and exhaust setting. The spectra were collected in soft ion sampling conditions using a low nozzle-skimmer declustering potential difference of 10 V.

Figure 6. Effect of aerosol carrier gas flow and exhaust flow rates on average cluster order (n) for a) $[Na_n(HCO_2)_{n+1}]^-$ and b) $[Na_n(HCO_2)_nNO_2]^-$ ions calculated using Equations 2 and 3.

Figure 7. Relative sensitivities (flow injection peak areas) of chlorine-containing ions detected in soft ion sampling conditions (nozzle-skimmer potential difference of 10 V) upon injection of chloramphenicol. Sensitivities are normalized to that of the most intense chlorinated ion ($[NaHCO_2{}^{35}Cl]^-$). Error bars indicate one standard deviation of the average based on triplicate injections.

Tables

Table 1 Operating parameters for ICP-based PARCI

Parameter	Value
Plasma gas	14 L/min
Auxiliary gas	1.2 L/min
RF power	1100W
Injector tip diameter	1.5 mm
Analyte nebulizer gas	1.25 SLPM
Reagent nebulizer gas	0.35 SLPM
Makeup gas	0-1 SLPM (0.2 SLPM optimum conditions)
Analyte solution flow rate	200 µL/min LC-MS water
Reagent solution	200 µM sodium acetate in LC-MS grade methanol
Reagent solution flow rate	30 µL/min
Exhaust velocity	3.8, 4.8, 5.8, 6.8 m/s (5.8 m/s optimum conditions)
Sampler	Flat aluminum orifice, 2 mm id, 1 mm thick
Sampling depth	9 mm downstream of the load coil
Reaction tube	50 mm stainless steel tube, ¼” o.d., 0.19” i.d

Table 2 Reaction thermochemistries calculated at the ωB97xD/aug-cc-pVTZ level

Number	Reaction	ΔH_{600K} (kJ/mol)	ΔG_{600K} (kJ/mol)
1	$HCO_2^- + NaHCO_2 \rightarrow [Na(HCO_2)_2]^-$	-196	-127
2	$NO_2^- + NaHCO_2 \rightarrow [NaHCO_2NO_2]^-$	-189	-120
3	$OCN^- + NaHCO_2 \rightarrow [NaHCO_2OCN]^-$	-156	-102
4	$Cl^- + NaHCO_2 \rightarrow [NaHCO_2Cl]^-$	-178	-128
5	$Cl^- + NaNO_2 \rightarrow [NaNO_2Cl]^-$	-191	-141
6	$NaCl + HCO_2^- \rightarrow [NaHCO_2Cl]^-$	-226	-157
7	$NaCl + NO_2^- \rightarrow [NaNO_2Cl]^-$	-219	-151
8	$NaCl + HCO_2^- \rightarrow Cl^- + NaHCO_2$	-48	-29
9	$NaCl + NO_2^- \rightarrow Cl^- + NaNO_2$	-27	-10
10	$NaCl + [Na(HCO_2)_2]^- \rightarrow [NaHCO_2Cl]^- + NaHCO_2$	-30	-30
11	$NaCl + [NaHCO_2NO_2]^- \rightarrow [NaNO_2Cl]^- + NaHCO_2$	-30	-30
12	$NaCl + [NaHCO_2NO_2]^- \rightarrow [NaHCO_2Cl]^- + NaNO_2$	-17	-17
13	$F^- + NaHCO_2 \rightarrow NaF + HCO_2^-$	-41	-57
14	$F^- + NaNO_2 \rightarrow NaF + NO_2^-$	-62	-76
15	$NaF + HCO_2^- \rightarrow [NaHCO_2F]^-$	-202	-134
16	$NaF + NO_2^- \rightarrow [NaNO_2F]^-$	-196	-128
17	$NaF + [Na(HCO_2)_2]^- \rightarrow [NaHCO_2F]^- + NaHCO_2$	-6	-7
18	$NaF + [NaHCO_2NO_2]^- \rightarrow [NaNO_2F]^- + NaHCO_2$	-7	-8
19	$NaF + [NaHCO_2NO_2]^- \rightarrow [NaHCO_2F]^- + NaNO_2$	+7	+6

Figures

Figure 1:

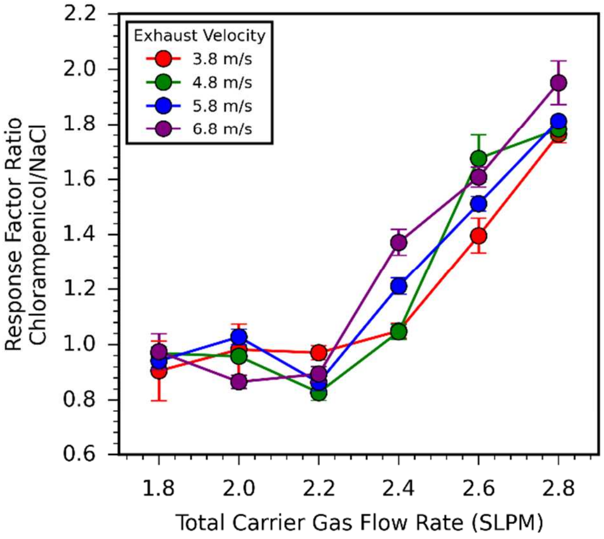

Figure 1. Ratio of Cl response factors from flow injections of NaCl and chloramphenicol as a function of carrier gas flow rate at various exhaust velocity settings. Error bars reflect one standard deviation of the average based on triplicate injections of each compound.

Figure 2:

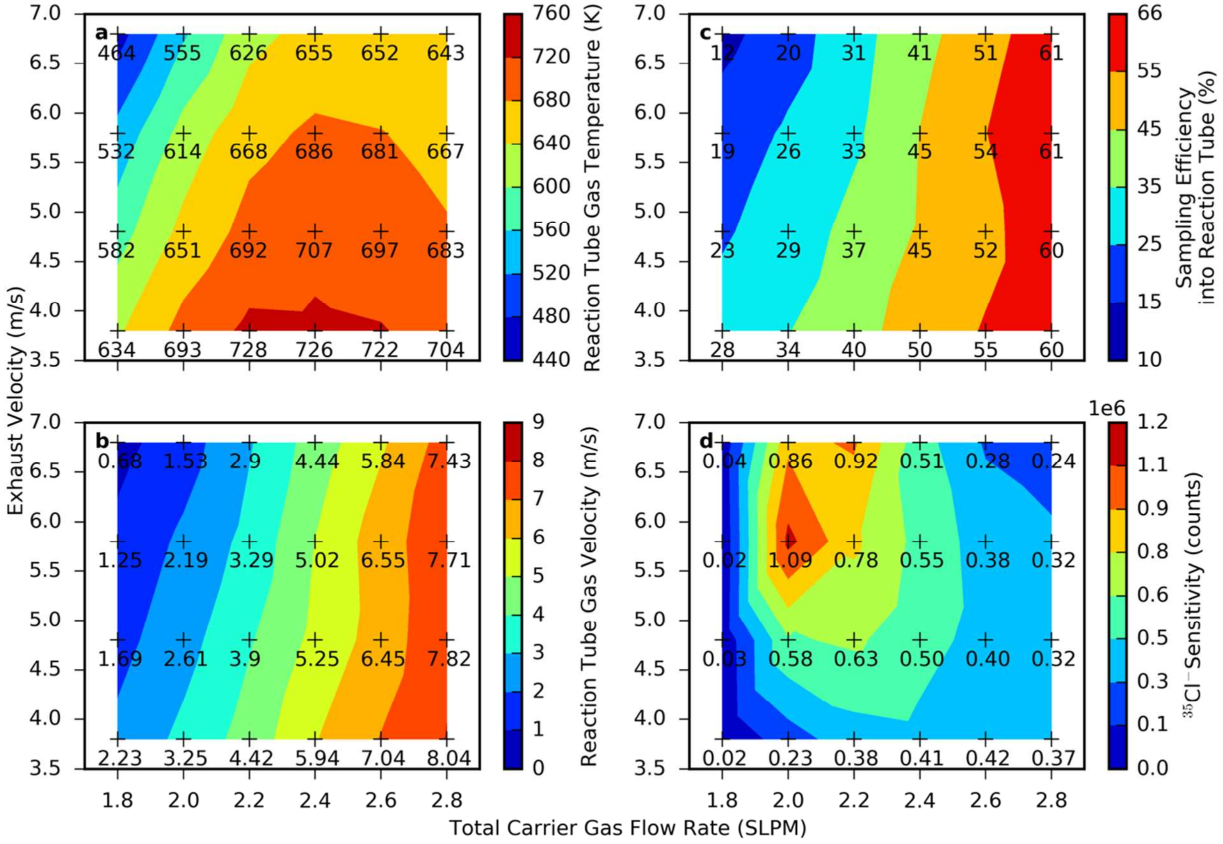

Figure 2. Effect of aerosol carrier gas flow rate and exhaust flow rate at 1100 W on a) temperature at reaction tube outlet, b) argon gas velocity flowing out of the reaction tube, c) sampling efficiency into the reaction tube calculated from the ratio of measured gas flow rate at the end of the reaction tube (Equation 1) to the total aerosol carrier gas flow rate, and d) Cl^- sensitivity measured as the average peak area from triplicate injections of 12.5 μM chloramphenicol. Contour plots are utilized to facilitate identification of trends using Delaunay triangulation and linear interpolation between the data points to color the contours. Experimental values are indicated at the grid points. A nozzle-skimmer potential difference of 130 V was used in experiments of Figure 2d to improve Cl^- detection sensitivity.

Figure 3:

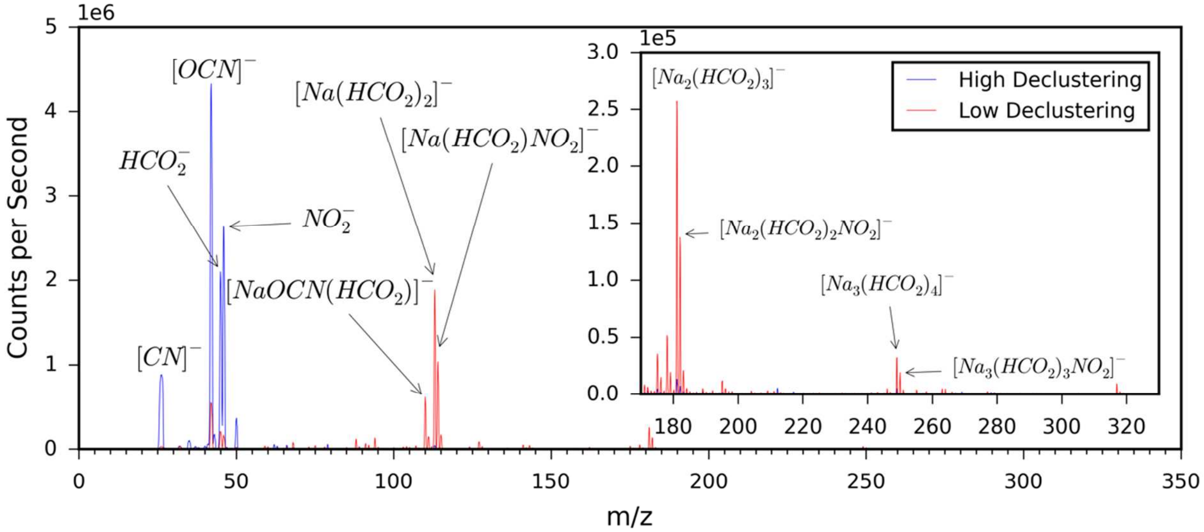

Figure 3. Effect of declustering potential on background ions at optimized ion source operating conditions for best Cl^- sensitivity (2.0 SLPM carrier flow rate, 5.8 m/s exhaust velocity, 1100 W RF power). The inset shows enlarged mass spectrum for the section with m/z > 170. Methanolic sodium acetate was used as ionization reagent. High declustering refers to 130 V potential difference between nozzle and skimmer of the MS while low declustering refers to 10 V potential difference.

Figure 4:

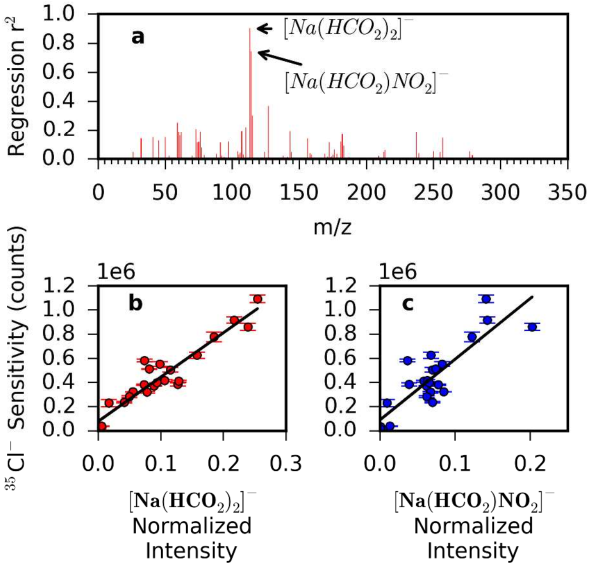

Figure 4. a) r^2 values for linear regression of background ions' normalized intensities (collected at low declustering nozzle-skimmer potential) with $^{35}Cl^-$ sensitivity (measured at high declustering potential) at carrier gas flow and exhaust flow rates identical to those in Figure 2. b) Correlation plots of normalized intensities for m/z 113 ($[Na(HCO_2)_2]^-$), and c) m/z 114 ($[NaHCO_2NO_2]^-$). The background ion intensities were normalized to the total ion counts in each spectrum.

Figure 5:

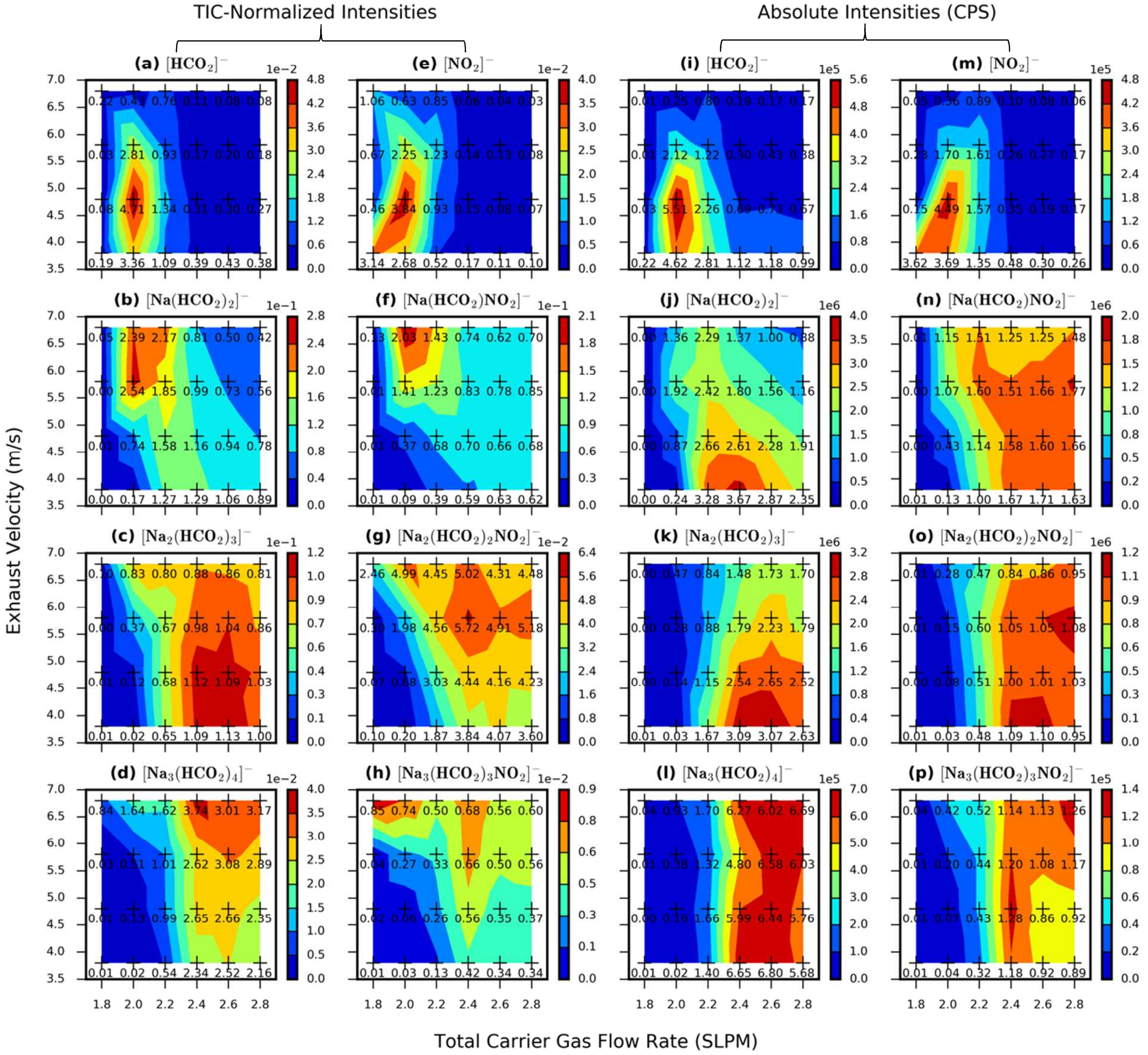

Figure 5. a-h) TIC-normalized and, i-p) absolute intensities of formate and nitrite ions and their clusters with sodium formate as a function of carrier gas flow rate and exhaust setting. The spectra were collected in soft ion sampling conditions using a low nozzle-skimmer declustering potential difference of 10 V.

Figure 6:

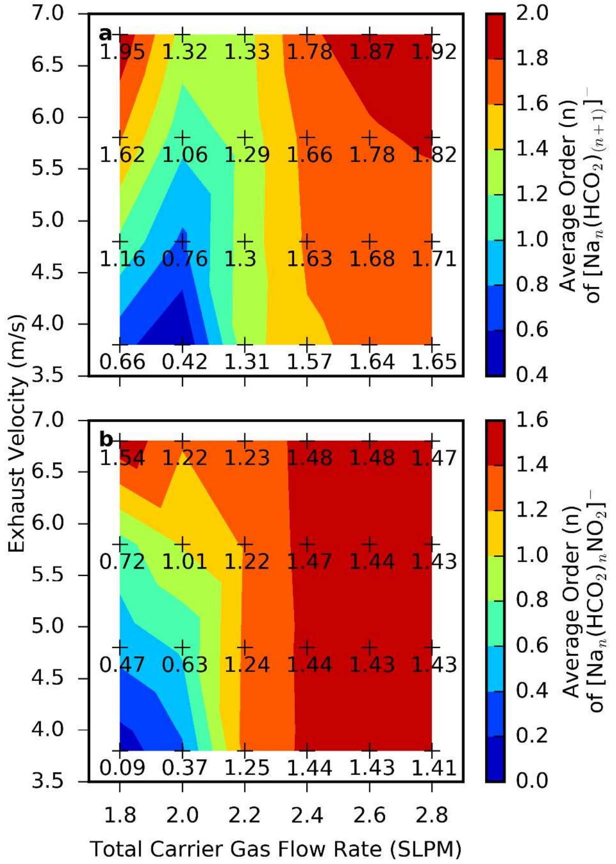

Figure 6. Effect of aerosol carrier gas flow and exhaust flow rates on average cluster order (n) for a) $[Na_n(HCO_2)_{n+1}]^-$ and b) $[Na_n(HCO_2)_nNO_2]^-$ ions calculated using Equations 2 and 3.

Figure 7:

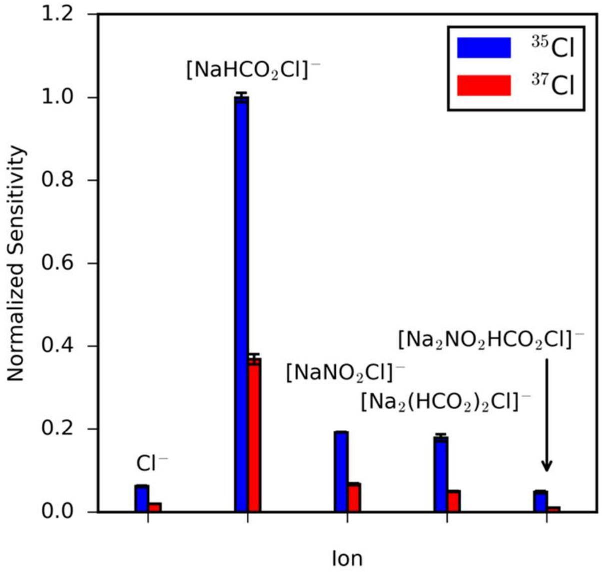

Figure 7. Relative sensitivities (flow injection peak areas) of chlorine-containing ions detected in soft ion sampling conditions (nozzle-skimmer potential difference of 10 V) upon injection of chloramphenicol. Sensitivities are normalized to that of the most intense chlorinated ion ([NaHCO$_2$^{35}Cl]$^-$). Error bars indicate one standard deviation of the average based on triplicate injections.

TOC graphical abstract:

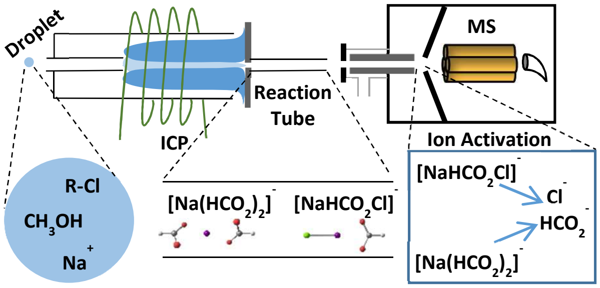

Detection of chloride ion from chlorinated compounds is influenced by cluster ion formation in the afterglow of an ICP.